Optical Fiber Technology 90 (2025) 104113

Contents lists available at ScienceDirect

Optical Fiber Technology

journal homepage: www.elsevier.com/locate/yofte

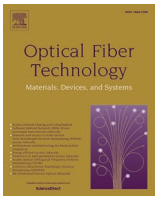

Regular Articles

AI-powered MMI fiber sensors for wide-range refractive index detection using neural networks algorithm

Nurul Farah Adilla Zaidi [a], Muhammad Yusof Mohd Noor [a,*], Nur Najahatul Huda Saris [a], Mohd Rashidi Salim [a], Sumiaty Ambran [b], Azizul Azizan [c], Raja Kamarulzaman Raja Ibrahim [d,e], Fauzan Ahmad [b], Nurul Ashikin Daud [a], Norazida Ali [f], Norizan Mohamed Nawawi [g], Ian Yulianti [h], Gang-Ding Peng [i]

[a] Faculty of Electrical Engineering, Universiti Teknologi Malaysia, 81310 Skudai, Johor, Malaysia
[b] Malaysian-Japan International Institute of Technology (MJIIT), Universiti Teknologi Malaysia, 54100 Kuala Lumpur, Kuala Lumpur, Malaysia
[c] Faculty of Artificial Intelligence, Universiti Teknologi Malaysia, 54100 Kuala Lumpur, Kuala Lumpur, Malaysia
[d] Department of Physics, Faculty of Science, Universiti Teknologi Malaysia, 81310 Skudai, Johor, Malaysia
[e] Laser Centre, Ibnu Sina Institute for Scientific and Industrial Research (ISI-SIR), Universiti Teknologi Malaysia, 81310 Johor Bahru, Johor, Malaysia
[f] Department of Electrical Engineering, Politeknik Mersing, 86800 Mersing, Johor, Malaysia
[g] Faculty of Electronic Engineering & Technology (FKTEN), Universiti Malaysia Perlis, 02600 Pauh Putra, Arau, Perlis, Malaysia
[h] Physics Department, Universitas Negeri Semarang, Sekaran, Gunungpati, Semarang, Central Java, Indonesia
[i] School of Electrical Engineering and Telecommunications, University of New South Wales, Sydney, Australia

ARTICLE INFO

Keywords:
Artificial intelligence (AI)
Neural Network (NN)
Regression
Refractive index fiber sensor
No-core fiber (NCF)
multimode interference (MMI)
machine learning (ML)

ABSTRACT

This research presents an artificial intelligence (AI)-driven machine learning (ML) approach for accurately measuring refractive index (RI) values across both lower and higher regimes than the fiber material's RI, using a simple single multimode interference (MMI) fiber sensor. The sensor configuration consists of a no-core fiber (NCF) segment between two single-mode fiber (SMF) sections. A Bilayer Neural Network (BNN) regression model is employed to predict both low refractive index (LRI) and high refractive index (HRI) regimes, achieving a broad dynamic measurement range from 1.3000 RIU to 1.3900 RIU for LRI regime and from 1.4600 RIU to 1.5500 RIU for HRI regime. The model demonstrates 99.7% accuracy and a low root mean square error (RMSE) of 0.0044, ensuring that predicted RI values closely match actual measurements without any RI ambiguity. Furthermore, the all-silica NCF structure is inherently resistant to temperature fluctuations, enabling its deployment in environments with varying temperatures without requiring additional temperature compensation mechanisms.

1. Introduction

RI sensors are essential tools in a wide range of fields, including chemical analysis [1,2], biomedical diagnostics [3,4], and environmental monitoring [5,6]. These sensors are used to detect changes in the RI of a medium, which can indicate the presence of specific substances or changes in environmental conditions. Notably, among various types of RI sensors, optical fiber sensors (OFS) have gained widespread attention due to their unique advantages, including compact size, high sensitivity, immunity to electromagnetic interference, and the ability to perform remote sensing [7–10]. As a result, these features make OFS particularly well-suited for applications that require precise measurements in challenging environments.

Recent advancements in OFS technology have significantly broadened their applications across diverse fields. In the biomedical sector, OFS have emerged as promising wearable devices, enabling real-time remote patient monitoring to meet the growing demand for continuous health data [11]. For instance, the recent study titled "Smart Photonic Wristband for Pulse Wave Monitoring" (OES 2024) demonstrates the ability of OFS to capture pulse wave data with high accuracy, supporting non-invasive health monitoring [12]. Additionally, the development of thermorefractometric OFS technology has enabled dual-function sensing, where a single device can simultaneously detect RI and temperature. This feature is particularly advantageous for monitoring sweat analytes and other biomarkers, offering potential for expanded applications in wearable health monitoring [13]. Such advancements

* Corresponding author.
E-mail address: yusofnor@utm.my (M.Y. Mohd Noor).

https://doi.org/10.1016/j.yofte.2024.104113
Received 3 October 2024; Received in revised form 18 November 2024; Accepted 23 December 2024
Available online 3 January 2025

underscore the potential of OFS in wearable healthcare, especially for monitoring RI changes linked to physiological and biochemical processes.

Beyond biomedical applications, OFS are widely utilized in various other sectors. In industrial monitoring, they contribute to structural health assessments by detecting minute changes in material's RI, which can indicate stress or damage [14]. In environmental sensing, OFS play a crucial role in monitoring water quality in real time, thereby aiding in pollution detection [15]. Furthermore, in agriculture, OFS support precision farming by monitoring soil and crop conditions, which enhances yield and sustainability through accurate measurements [16]. This broad spectrum of applications underscores the versatility of OFS and the ongoing demand for technological advancements to enhance their performance, especially for accurate measurements across diverse environmental conditions.

Building on this foundation, various OFS types have been developed specifically for RI sensing, each leveraging different mechanisms to meet diverse application needs. Commonly employed techniques include surface plasmon resonance (SPR) [17,18], interferometry [19,20], fiber gratings [21,22], tapered fibers [23,24], and MMI [25,26]. While these methods offer valuable solutions for RI detection, most OFS are optimized for the LRI regime, where the RI of the external medium is lower than the fiber core, typically below 1.4500 RIU [27,28]. In this LRI regime, light remains confined within the fiber core. However, when the RI of the external medium surpasses that of the fiber core, entering the HRI regime above 1.4500 RIU, some of the light escapes from the fiber due to the RI mismatch. This phenomenon, known as leaky mode, results in ambiguous and unreliable sensor output during the transition from LRI to HRI regimes, thereby restricting the sensor's effective detection range to LRI regime only.

Given the growing demand for versatile RI sensors capable of detecting both LRI and HRI regimes, several method have been explored. One approach is the use of a single-cavity Fabry-Perot interferometer (FPI), which detects LRI and HRI regimes based on Fresnel reflection at the fiber tip. These sensors measure phase shifts in the interference spectrum, enabling a wide RI detection range from 1.0000 RIU to 2.0000 RIU [29]. Additionally, a dual-cavity FPI sensor configuration has been developed, utilizing two air cavities to provide accurate RI measurements across a range from 1.3924 RIU to 1.5882 RIU using Fourier Transform (FT) signal demodulation. While these sensor designs are capable of sensing both LRI and HRI regimes, they increase the complexity of sensor fabrication and signal demodulation [30]. To address this, the same researchers have employed AI classification ML algorithm for demodulating the FPI sensor signal, facilitating RI sensing across both LRI and HRI regimes (1.3158 RIU to 1.5809 RIU). Although this approach simplifies signal demodulation, the complexity of the sensor structure remains high and inherently sensitive to temperature changes.

One promising alternative for the simple sensor structure of OFS RI sensing is the use of MMI structures based on NCF. These MMI structures offer several advantages, including increased flexibility, reduced cost, enhanced sensitivity, and simplified fabrication. However, the MMI sensor can only detect LRI [31] and HRI [32] individually, requiring the use of two separate MMI-based sensors with NCF. This is due to challenges with RI ambiguity caused by the different mechanisms of guided modes in the LRI regime and leaky modes in the HRI regime.

Therefore, for this study, we introduce a novel approach that integrates AI with an MMI fiber sensor using NCF structure to enable both LRI and HRI regimes sensing with a single MMI sensor. The sensor design comprises a short NCF segment spliced between two SMF segments. The sensing mechanism utilizes both guided and leaky modes within the MMI structure. The demodulation process uses an AI-based regression BNN algorithm, which facilitates LRI and HRI regimes detection. In the BNN model, the first layer processes raw sensor data which are the full transmission spectrums obtained from each RI measurement in the experiment. The second layer refines these features, capturing complex patterns and non-linear relationships. This multi-layered architecture enables the BNN to accurately predict RI values across both LRI and HRI regimes. Our results show that this approach effectively resolves the ambiguity issues commonly found in MMI sensors for both LRI and HRI regimes sensing applications. The simplicity of the sensor structure improves the overall robustness and stability of the sensing system. Moreover, the all-silica design of the MMI sensor makes it inherently resistant to temperature fluctuations which eliminates the need for additional temperature compensation mechanisms.

2. Principle

2.1. Neural networks

Neural networks (NNs) are advanced computational frameworks inspired by biological neural systems, where interconnected nodes operate as processing units linked by adjustable weights, denoted as w_n. Each node receives input signals (X_n), applies them to an activation function (f), and generates corresponding output signals. The structural configuration of an NN, defined by the number of layers and the nodes within each layer, significantly influences its ability to model complex, nonlinear data patterns [33]. While single-layer perceptrons (SLPs) provide the foundation for NN, they exhibit limited capacity for feature representation. Conversely, multi-layer perceptrons (MLPs) offer enhanced modelling power by leveraging multiple layers to learn hierarchical feature representations and capture intricate dependencies within the data. In this study, a BNN is proposed for predicting RI signals. The BNN employs a two-hidden-layer MLP architecture, which is particularly effective for modelling nonlinear relationships present in the dataset [34]. This architecture enables the network to capture both fundamental and sophisticated interactions within the data. The first hidden layer extracts critical spectral features from the transmission spectrum, forming the initial foundation for feature processing. Subsequently, the second hidden layer further refines these features, uncovering more nuanced and complex patterns essential for accurate RI prediction. This hierarchical design ensures comprehensive feature extraction, resulting in improved predictive accuracy [35].

Notably, the BNN is trained using the backpropagation algorithm, an iterative optimization technique that minimizes prediction errors by adjusting the network's weights. By employing the complete transmission spectrum of the sensor as input, the network effectively captures the intricate relationship between transmission wavelengths and the RI signal. This systematic approach allows the BNN to model high-order interactions within the data, leading to highly reliable RI predictions across a wide range of values. Therefore, the robustness of the BNN's architecture is reflected in its ability to process complex data dependencies and produce consistent with precise predictions. As depicted in Fig. 1, the model comprises an input layer (X_n), a first hidden layer ($H1_n$), a second hidden layer ($H2_n$), and an output layer (RI_n). This configuration ensures that the BNN efficiently addresses the complexities of RI signal prediction while maintaining robust and consistent performance, thereby providing a reliable solution for real-world applications.

2.2. Multimode interference (MMI) in RI sensing

To explain MMI effectively, we utilize the conventional single-mode multimode single-mode (SMS) fiber sensor concept as the MMI device. In this proposed work, a NCF serves as the MMI structure. The fundamental mode of a SMF exhibits a circular symmetric characteristic, allowing the field distribution of the light launched from the SMF to be represented as E_{in}. When light enters the NCF, the input field decomposes into eigenmodes LP_{nm}, where n and m refer to modes in the longitudinal and transverse directions, respectively. Due to the circular symmetry of the input field and assuming ideal axial alignment between the SMF and NCF cores, only the LP_{0m} modes are excited within the NCF

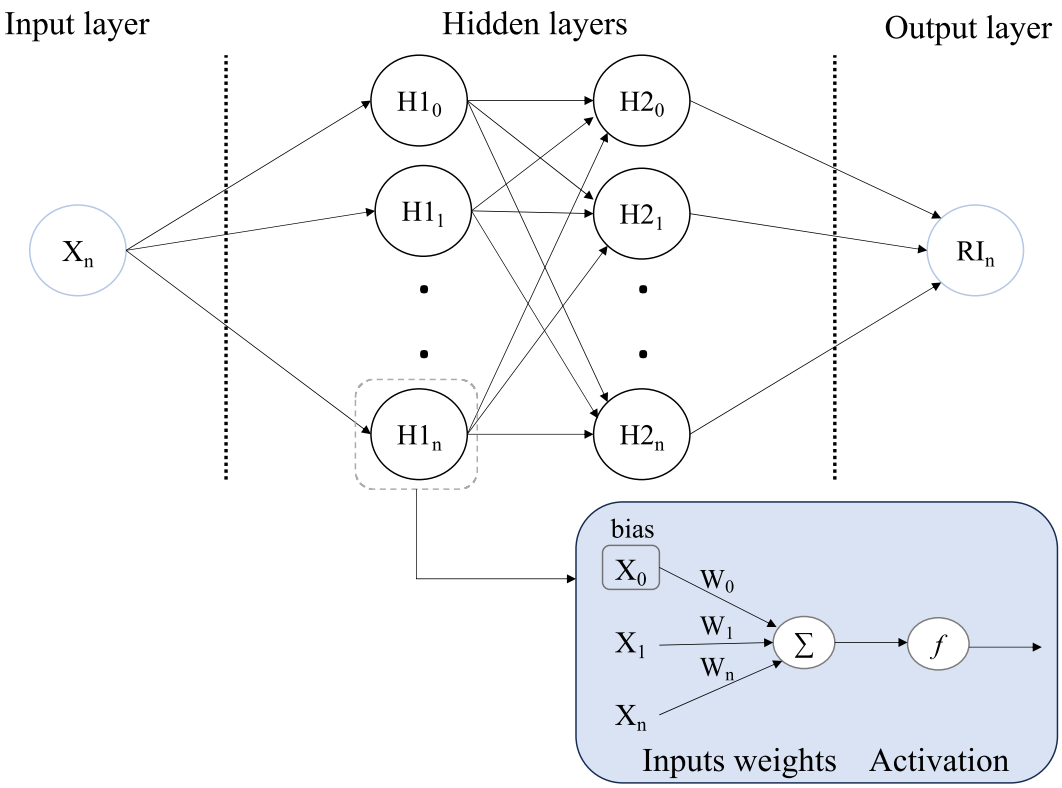

Fig. 1. Bilayer Neural Network (BNN) structure.

section [36]. Representing the field profile of LP_{0m} as E_m, the eigenmodes of the NCF are normalized as follows:

$$\int_0^\infty |E_{in}|^2 ds = \int_0^\infty |E_m|^2 ds \tag{1}$$

$m = 1, 2, \cdots,$

Neglecting the minor radiation escaping from the NCF, we have:

$$E_{in} = \sum_{m=1}^{M} n_m E_m \tag{2}$$

where n_m is the excitation coefficient for each eigenmode, expressed through the overlap integral between E_{in} and E_m:

$$n_m = \frac{\int_0^\infty E_{in}.E_m ds}{\int_0^\infty E_m.E_m ds} \tag{3}$$

A higher coupling coefficient indicates a mode with greater power. As the light travels through the NCF section, it becomes possible to calculate the modal interference field at a propagation distance along the NCF, z, from the input as:

$$E(z) = \sum_{m=1}^{M} n_m E_m e^{i\beta_m z} \tag{4}$$

where β_m represents the propagation constant for each eigenmode propagating through the NCF. The interference modes along the NCF remain in guided mode when the surrounding RI is lower than that of the NCF structure, a condition referred to as the LRI regime. Conversely, if the surrounding RI exceeds that of the NCF sensing element, known as the HRI regime, the fiber section transitions into a leaky waveguide. In this case, the light leaks out instead of facilitating guided MMI. This leaky structure supports a continuous spectrum of radiation modes, causing the light to propagate longitudinally with attenuated amplitude while concurrently leaking transversely. The primary mechanism for RI sensing in this leaky structure involves monitoring the attenuations of leaky modes within the NCF [37].

Besides, when there is a change in the index distribution across the transverse direction, the propagation constant becomes complex within the leaky section. The real part of this complex propagation constant is similar to the propagation constant in the SMF, while the imaginary part indicates the attenuation constant, defining the leaky nature of the corresponding modes. Given that the field in the NCF results from the modal interference of all excited leaky modes with varying propagation constants, the field distribution at a specific propagation distance, z, can be expressed as follows [38]:

$$E(z) = \sum_{m=1}^{M} n_m E_m e^{i\beta_m z} e^{-\alpha_m z} \tag{5}$$

here, E_m denotes the electric field of the mth leaky mode in the NCF, while β_m and α_m representing the propagation constant and attenuation constant of the mth leaky mode, respectively. Generally, high-order leaky modes with greater attenuation constant than low-order modes would leak out rapidly to the surrounding. Hence, only a few low-order modes contribute to the output after some characteristic levels. The remaining leaky modes should have approximately the same β. The transmission spectra at the output cross-section of the NCF should display as in (6). The overlap integral of modal fields due to longitudinal coupling between leaky modes in silica rod and guided mode in SMF can determine the normalized output intensity (I_{out}) of the SNS fiber structure.

$$I_{out} = 10log_{10}\left(\left|n_m^2 e^{i\beta_m z} e^{-\alpha_m z}\right|^2\right) \tag{6}$$

Hence, the normalised output intensity at output cross section $z = L$ is given by [37]:

$$I_{out}(L) = 10log_{10}\left(\frac{|\int E(L).E_{out}ds|^2}{\int |E(L)|^2 ds \int |E_{out}|^2 ds}\right) \quad (7)$$

where E_{out} represents the fundamental mode in the output SMF. If the input and output SMFs are identical, E_{out} equals E_i.

The interference of guided modes in the LRI regime and leaky modes in the HRI regime generates a series of power peaks and dips, creating a characteristic MMI pattern influenced by the surrounding RI and mode attenuation. In the LRI regime, when the surrounding RI is significantly lower than that of the NCF, the NCF effectively guides light, resulting in strong total internal reflection and a well-defined MMI pattern. This produces a strong and distinct interference signal, with modes in the NCF RI interacting as expected, generating a clear and robust interference pattern at the output SMF. However, as the surrounding RI approaches the NCF RI, light confinement weakens, leading to increased power leakage into the surrounding medium. Consequently, the MMI effect becomes less efficient, and the interference pattern diminishes, particularly when the surrounding RI exceeds the NCF RI in the HRI regime.

3. Experimental setup

The experimental setup for the MMI's NCF sensor involved a simple and straightforward fabrication process. To begin, a 125 μm diameter no-core fiber (NCF, F300, Flexiliate Sdn. Bhd) was spliced between two single-mode fibers (SMF, SMF-28, Thorlabs) using a fusion splicer (Fujikura, CT-30) in automatic mode to ensure precise alignment and minimal splice loss. The NCF segment was then cleaved to a length of 3.5 cm, chosen based on its ability to optimize sensor performance by enhancing the MMI effect. A clean and flat end face of the output SMF was subsequently spliced to the NCF, completing the MMI-based sensor structure. The 3.5 cm length of the NCF was selected based on initial testing, which revealed two key spectral features in the 1500 nm – 1600 nm wavelength range, which are a deep dip indicating an attenuation band and a sharp peak representing a transmission band. These characteristics were crucial for the sensor's effectiveness in detecting changes in the RI across a broad range.

For sensor characterization, a broadband light source (BLS), specifically an Amplified Spontaneous Emission (ASE) source, was coupled into the sensor, and the output was analyzed using an optical spectrum analyzer (OSA) as in Fig. 2. The sensor's RI sensitivity was evaluated using calibrated RI liquids from the Cargille Series, which included Series A and AAA. These liquids covered RI values ranging from 1.3000 RIU to 1.3900 RIU for LRI regime sensing and from 1.4600 RIU to 1.5500 RIU for HRI regime sensing. The liquids were carefully applied to the NCF sensor, allowed to stabilize for several minutes and the resulting output spectrum was recorded. After each measurement, the RI liquid was meticulously removed using dry tissue, and the sensor was cleaned with alcohol and air-dried to ensure no residue remained. This cleaning procedure was repeated between each application of different RI liquids, ensuring consistency and preventing cross-contamination. Measurements were conducted across the entire LRI and HRI regimes, and all data were recorded.

Furthermore, the RI of the NCF was referenced to the RI of pure silica, which is approximately 1.4440 RIU at a wavelength of 1550 nm. RI liquids with values below this reference were categorized as LRI regime, while those above were classified as HRI regime. The sensor was securely mounted on a microscope glass slide, with adhesive tape applied on both sides to prevent movement or bending. This ensured that the sensor remained free from any external strain and bending that could potentially influence the accuracy of the measurements.

4. Results and Discussion

4.1. Sensor characterization

In this study, the transmission characteristics of the NCF sensor were thoroughly investigated under different RI environments, ranging from LRI to HRI regimes conditions. The experiments were conducted at a constant room temperature to ensure the stability of the transmission response, isolating the impact of RI variation on the sensor's performance. This approach eliminates any external temperature-related influences on the sensor's transmission spectrum, providing a clearer understanding of its RI sensitivity. Fig. 3 illustrates the transmission spectrum response of the NCF sensor in both the LRI and HRI regimes, along with the transmission profile of the broadband light source (BLS).

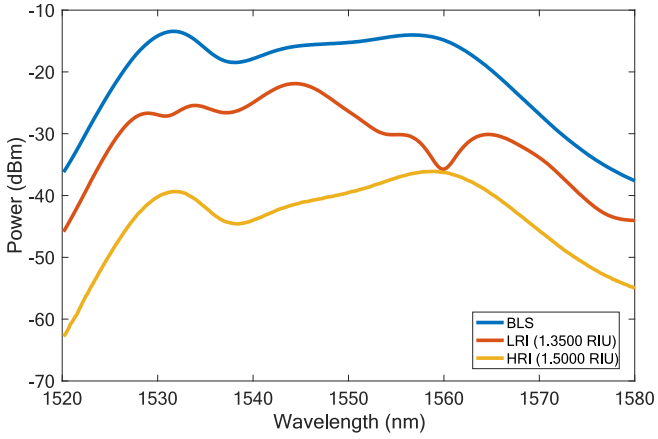

Fig. 3. Transmission spectrum response of the NCF Sensor in LRI and HRI regimes.

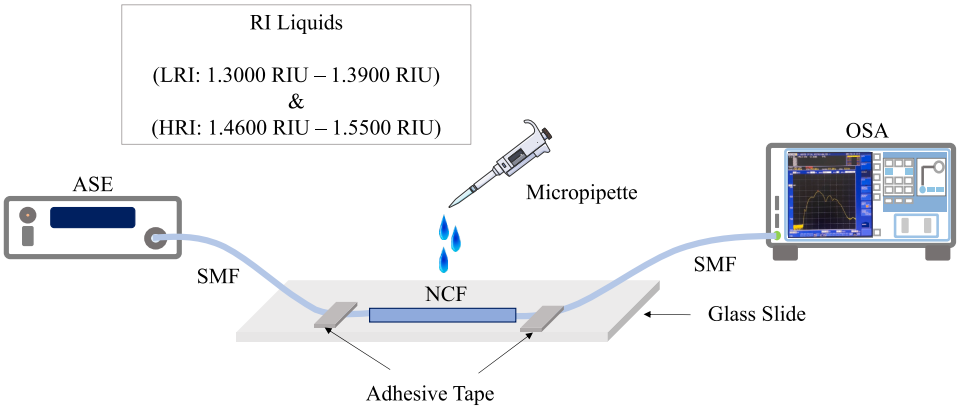

Fig. 2. Experimental setup for measuring LRI and HRI using a NCF sensor.

In this context, BLS refers to the spectral output profile of the light source itself. Hence, notable changes are observed in the transmission modes of the MMI sensor when transitioning between the LRI and HRI regimes. In the LRI regime, there is a distinct attenuation and transmission band in the transmission mode. However, in the HRI regime, these bands become less defined, resembling the transmission profile of the BBS as depicted in Fig. 3. This behaviour is due to the higher-order modes experiencing a significant loss in the HRI regime but a lower loss in the LRI regime, as evidenced by the Fast Fourier Transform (FFT) signals for both regimes shown in Fig. 4.

Fig. 4 illustrates the FFT results for the transmission mode of the sensor operating in both LRI and HRI regimes. In this figure, several dominant peaks appear in the spatial frequency spectra, indicating that the interference involves multiple modes. The lowest mode represents the fundamental mode, while the higher-order modes can be divided into dominant and weakly higher-order modes. The interference between the fundamental mode and higher-order modes produces an MMI pattern spectrum, resulting in a clear dip spectrum in the LRI regime. However, in the HRI regime, the higher-order modes experience more power losses due to the HRI, causing minimal interference between the fundamental mode and the higher-order modes. This diminishes the MMI pattern, as shown in Fig. 3. When the surrounding RI is higher than that of the core of the fiber, light becomes less confined within the core, leading to a reduction in the peak power of the lowest mode. Consequently, the MMI pattern diminishes because the interference is weaker in the HRI regime. In the HRI regime, higher-order modes undergo substantial loss, diminishing their power output and limiting the MMI effect.

Fig. 5 presents the inset graph showing LRI regime variations in the wavelength range of 1555 nm to 1570 nm, illustrating how the sensing spectra change as the analyte RI increases. Both intensity changes and wavelength shifts are evident as the sensor interacts with the analyte RI, with the shifts becoming more pronounced as the analyte RI nears the NCF RI. As the analyte RI increases, the contrast between the analyte and NCF RIs decreases, leading to greater penetration depth and increased light interaction between the NCF and the analyte. This enhances the sensor's sensitivity, causing more significant intensity changes and wavelength shifts.

In contrast, Fig. 6 shows the inset graph corresponding to the HRI regime variation within the wavelength range of 1555 nm to 1570 nm. As the analyte RI increases, the sensor predominantly exhibits intensity changes, with minimal wavelength shift. The signal-to-noise ratio (SNR) is reduced compared to the LRI regime's condition, likely due to the transition from discrete guided modes to leaky waveguide modes. Instead, the NCF sensor begins to support leaky waveguide modes, which results in a broader, less distinct spectral profile. A key

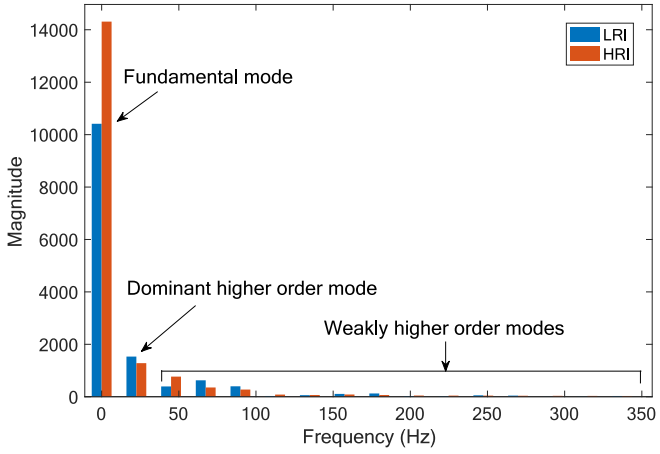

Fig. 4. Fast Fourier Transform (FFT) of the transmission mode of the sensor in LRI and HRI regimes.

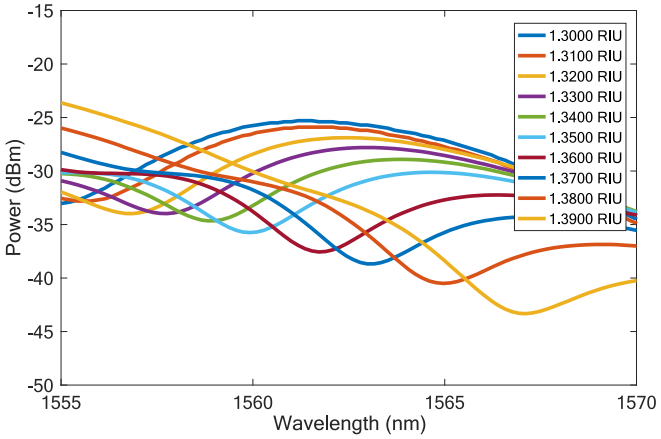

Fig. 5. Inset graph illustrating intensity changes and wavelength shifts in the LRI regime within the wavelength range of 1555 nm and 1570 nm.

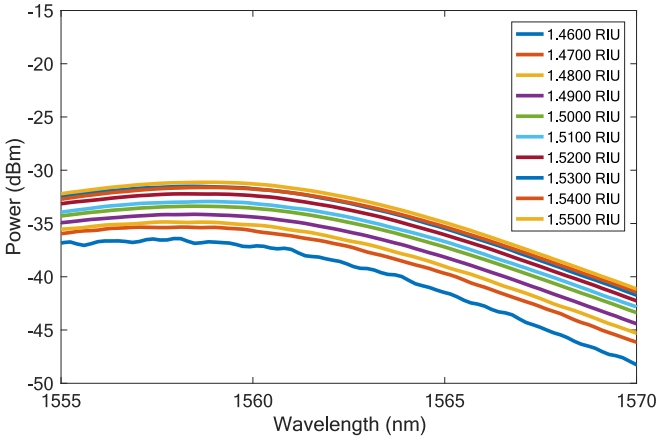

Fig. 6. Inset graph illustrating intensity changes in the HRI regime within the wavelength range of 1555 nm and 1570 nm.

observation in the HRI regime was the recovery in power coupling strength as the RI of the external medium exceeded that of the fiber core material. This phenomenon is explained by the confinement of leaky modes, which become more pronounced as the external RI increases. As the index approaches and surpasses the fiber core's RI, the mode overlap between the guided light and the external medium becomes more significant, resulting in enhanced power coupling and stronger transmission signals.

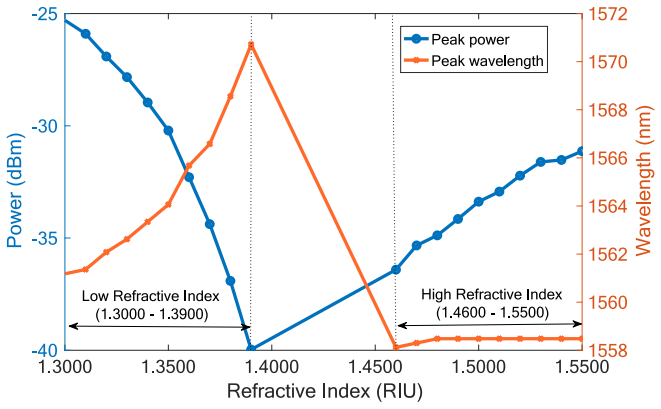

Fig. 7. Observed changes in wavelength shifts and intensity for both LRI and HRI environments.

Fig. 7 presents the observed changes in wavelength shifts and intensity for both LRI and HRI environments. The wavelength shift measurements show a linear relationship only within the LRI environment, with minimal shifts noted in the HRI environment. On the other hand, power change measurements reveal a distinct linear trend across the entire ranges from LRI to HRI regimes however, the responses from different RI values overlap, creating interpretative challenges. This overlapping effect is a recognized ambiguity issue with MMI sensors, which limits the effectiveness of traditional approaches in accurately analyzing sensor data throughout the full RI spectrum.

4.2. Spectral analysis with Neural networks

In traditional approaches to analysing the transmission spectra of MMI-based sensors, spectral dips or peaks are typically monitored to detect wavelength shifts or intensity changes. However, this method faces significant challenges when dealing with complex spectra, especially when overlapping features make it difficult to track shifts or intensity changes or variations at specific wavelengths. To overcome this, utilizing the entire transmission spectrum across multiple wavelengths offers a more accurate solution for sensing. The proposed BNN algorithm uses the full transmission spectrum as input data, with each transmission at sampled wavelengths treated as a feature variable in the input data array. This AI-based regression model then predicts the RI signal based on this input spectrum. Prior to making predictions, the input data is processed hierarchically through two hidden layers to accurately predict the RI signal.

In the experiment, 200 spectral responses were collected from the MMI sensor, corresponding to RI variations ranges from 1.3000 RIU to 1.3900 RIU and 1.4600 RIU to 1.5500 RIU, across 10 measurement cycles. These responses provided a total of 3,340 input sampling points, with each spectrum containing 334 wavelength sampling points at 0.18 nm intervals, covering the range from 1520 nm to 1580 nm. To train the model, 80 % of the data samples were randomly selected using the cv-partition function, while the remaining 20 %, which the model had not seen during training, were used to test the performance of the trained NN regression model. The BNN training process was implemented using MATLAB R2024a.

To evaluate the repeatability of RI measurements, one sample from both the LRI and HRI regimes was selected at 1.3800 RIU and 1.4800 RIU, respectively, at a wavelength of 1550 nm. The results are displayed in Fig. 8 as a bar graph. The corresponding statistical parameters related to repeatability characteristics are detailed in Table 1. For the LRI regime, a standard deviation (SD) of 0.33665 indicates a small deviation

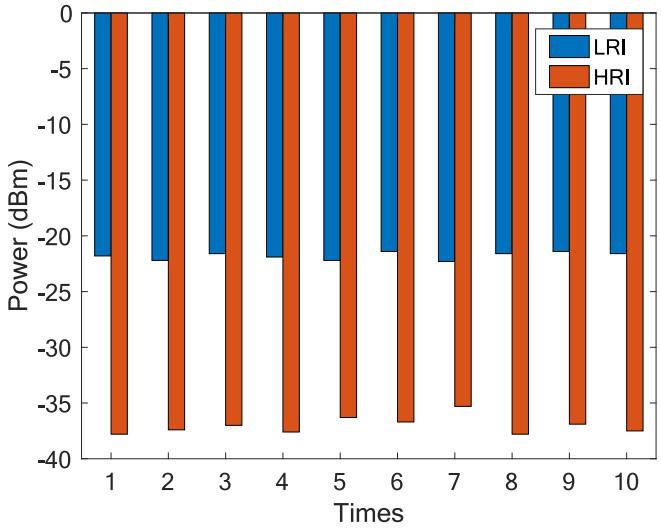

Fig. 8. Graph bar showing RI sample at LRI and HRI regimes for 1550 nm.

Table 1
Statistical parameters related to repeatability characteristic.

Statistical parameters	LRI	HRI
Standard Deviation (SD)	0.33665	0.78323
Variance (V)	0.11333	0.61344
Coefficient of Variation (CV)	0.015443 (1.5443 %)	0.021151 (2.1151 %)

LRI = Low refractive index, HRI = High refractive index.

from the mean, signifying that the measurements are tightly clustered. An SD of less than 1 is typically regarded as very good, reflecting minimal variability and high measurement precision. In contrast, for the HRI regime, the SD is 0.78323, indicating slightly higher variability, but still within an acceptable range, confirming consistency in the measurements. The relationship between variance (V) and SD, where variance is the square of the SD, shows that the HRI variance is larger than that of the LRI, suggesting greater data dispersion in the HRI regime. However, a variance value of 0.61344 for the HRI still reflects a limited spread in the data. The coefficient of variation (CV), which measures relative variability in relation to the mean, is low for both RI regimes, with the LRI having a slightly lower CV than the HRI. This indicates that both sets of measurements exhibit good repeatability, with the LRI regime displaying slightly higher consistency.

Fig. 9 demonstrates the strong predictive capability of the BNN regression model by comparing the predicted RI values with the actual observed RI values. The x-axis represents the actual RI values recorded during the experiment, while the y-axis shows the corresponding predicted RI values generated by the BNN model. The close clustering of data points around the identity line (where predicted values equal actual values) indicates a high level of accuracy in the model's predictions. Moreover, the minimal deviations from the identity line suggest that prediction errors were small and remained within an acceptable range, confirming the model's reliability. The consistency of these small deviations across the entire ranges of RI values further demonstrates that the model is not biased toward any specific RI ranges and can generalize well across both LRI and HRI regimes. In addition, the tight alignment of points around the identity line implies that the model captured the underlying relationships between the sensor's spectral responses and the RI variations effectively. This accuracy is crucial for sensing

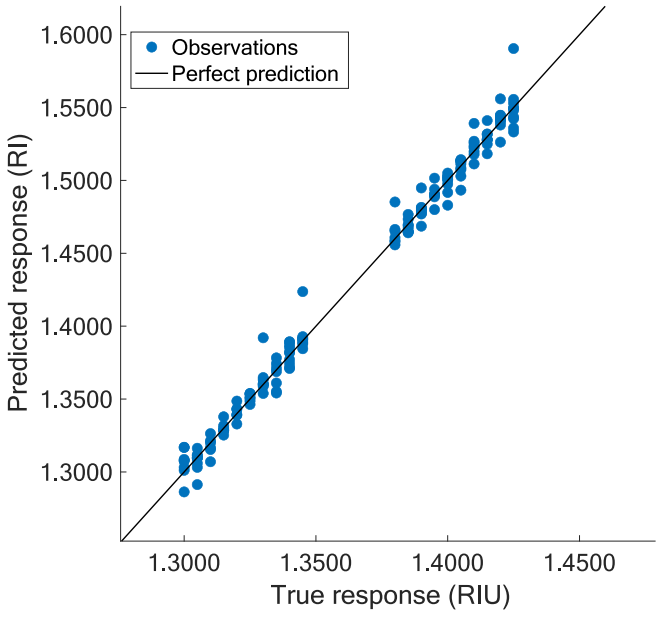

Fig. 9. BNN training regression model highlighting the comparison of predicted and observed RI values.

applications, where precision is essential for real-world implementation. The overall performance of the regression model, as visualized in the plot, highlights its potential for practical sensing applications, demonstrating not only strong prediction accuracy but also robustness across different RI environments. This result suggests that the BNN model can serve as a reliable tool for enhancing the performance of MMI fiber sensors in diverse RI sensing scenarios.

To evaluate the performance of the BNN model, a response plot was generated, comparing the predicted RI values against the sequence of recorded observations, represented by the record numbers. This response plot as illustrated in Fig. 10, provides a visualization of the model's predictive accuracy over time and across various data samples. The response plot exhibits a consistent alignment between the predicted RI values and the chronological order of the observations. This alignment is crucial because it reflects the model's capacity to accurately predict RI signal in the correct temporal sequence, ensuring that the model's performance remains reliable throughout the entire dataset. A well-aligned response plot indicates that the BNN model has successfully learned the underlying patterns in the data, allowing it to generate predictions that are not only accurate but also properly ordered. This consistent alignment is particularly important in practical sensing applications, where the sensor must continuously monitor changes in the RI in real-time.

In addition. the plot's well-organized display of predicted values shows that the model maintains its performance without significant deviations or outliers, which would otherwise indicate prediction errors or instability. The smooth progression of predicted RI values over the sequence of records suggests that the model is robust and capable of handling various input scenarios without losing accuracy. The effectiveness of the chronological alignment seen in the response plot also underscores the BNN's ability to generalize well across the entire dataset. This means that the model does not simply memorize specific data points but instead captures the broader trends and relationships in the data. Such generalization is crucial for ensuring that the model can perform accurately when faced with new, unseen data, which is a key requirement for practical deployment in real-world sensing environments. Furthermore, the orderly arrangement of predicted values corresponding to the record numbers signifies that the model has achieved a stable and consistent level of performance. This stability is an essential attribute for any sensor system, as it ensures that the sensor can be relied upon to deliver accurate RI measurements.

Besides that, Fig. 11 presents a residuals plot for the predicted RI values, highlighting the differences between the actual RI measurements and the predictions generated by the BNN model. This plot is crucial for understanding how well the model performs in capturing the underlying patterns in the data. The residuals, which are the differences between the observed and predicted values, are plotted against the predicted RI values. A key observation from the plot is the random scatter of residuals around the zero line across the entire ranges of predicted RI values. This

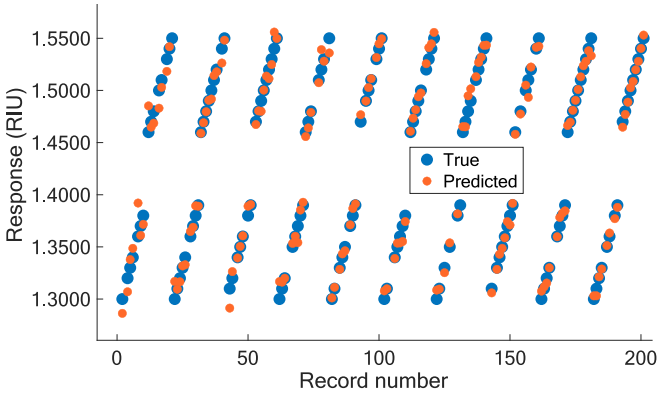

Fig. 10. Predicted RI values against record number.

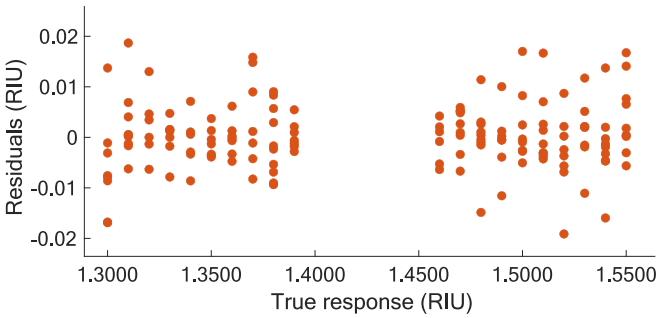

Fig. 11. Residual Plot of RI data.

randomness indicates that the BNN model effectively captures the variability in the data and that the prediction errors are not systematically biased in any direction. The lack of a discernible pattern or trend in the residuals suggests that the model has successfully learned the complex relationships between the sensor inputs and the refractive index values. Moreover, the absence of any structure in the residuals confirms that the key assumptions underlying the model, such as linearity and constant variance of the residuals (homoscedasticity), are satisfied. This is a crucial finding, as it supports the validity and robustness of the regression model. If a pattern had been observed in the residuals such as a funnel shape indicating increasing variance or a curvature suggesting nonlinearity, it would have signaled potential issues with the model's fit, such as heteroscedasticity or an inadequate representation of the data's true nature. The residual plot also gives understanding into the reliability of the model across different ranges of RI values. Since the residuals are consistently scattered without any significant deviation from the zero line, it can be inferred that the model performs well across both LRI and HRI values. This reinforces the conclusion that the BNN model generalizes effectively across the entire dataset, making it a robust tool for accurate RI sensing.

Table 2 presents an overview of the training performance of NN architectures commonly applied in AI-driven regression approach which are Narrow Neural Network, Medium Neural Network, Wide Neural Network, and Bilayer Neural Network. The performance of each model was evaluated using metrics such as Root Mean Squared Error (RMSE), Mean Squared Error (MSE), Mean Absolute Error (MAE) and R-squared (R^2), which were computed using MATLAB's regression learner tools. A model with lower RMSE, MSE, and MAE values demonstrates greater predictive accuracy, as these metrics suggest a closer alignment between predicted and actual values. Conversely, higher R2 values, approaching 1, signify that the model fits the data more accurately. The findings reveal that the BNN outperforms the other architectures across all evaluation criteria, achieving a regression accuracy of 99 %. This is primarily due to the BNN's more advanced structure, which includes multiple layers specifically two layers with few neurons each. These additional layers enhance the model's ability to identify and represent complex patterns and hierarchical relationships within the data for better accuracy. On the other hand, Narrow and Medium Neural Networks are characterized by simpler designs, often comprising a single layer or fewer neurons, which restricts their capacity to capture complex relationships. While the Wide Neural Network contains more neurons

Table 2
Evaluation of training accuracy across different neural network model.

Model	RMSE	MSE	MAE	R^2
Narrow Neural Network	0.0093170	8.6806E-05	0.006174	0.98828
Medium Neural Network	0.018959	0.00035946	0.010038	0.95147
Wide Neural Network	0.046242	0.0021383	0.0259	0.71133
Bilayer Neural Network	0.0083925	7.0435E-05	0.0054670	0.99049

RMSE = Root Mean Squared Error, MSE = Mean Squared Error, MAE = Mean Absolute Error, R^2 = R-squared.

within a single layer, it lacks the layered depth found as in the BNN. This absence of hierarchical processing limits its ability to refine and capture intricate data patterns, resulting in lower performance when compared to the BNN.

To further investigate the BNN's performance, Shapley values are utilized to provide a transparent and detailed interpretation of feature contributions. This approach decomposes each prediction into contributions from individual features, showing into how specific wavelength features influence the model's accuracy. In the context of predicting RI values, Shapley values are instrumental in understanding the impact of various wavelength features. The study examines Shapley explanations in two distinct scenarios which are LRI at 1.3000 RIU, as shown in Fig. 12, and HRI at 1.5500 RIU, as shown in Fig. 13. The analysis focuses on the top 10 wavelength features in each scenario to reveal their effects on prediction accuracy.

For the LRI condition, with an actual RI value of 1.3000 RIU, the model's prediction of 1.3003 RIU demonstrates minimal deviation, largely attributed to positive contributions from key features such as 1559.74 nm, 1566.90 nm, 1559.02 nm, and 1564.42 nm. These features exhibit significant positive Shapley values, indicating their critical role in enhancing the accuracy of low RI predictions by capturing essential spectral variations. Conversely, features such as 1543.00 nm, 1529.32 nm and 1545.88 nm, which exhibit negative Shapley values, detract from the model's accuracy. These negative contributions suggest that these features are less effective in LRI prediction, possibly due to their sensitivity to higher RI values.

While in the HRI scenario, where the actual RI value is 1.5500 RIU, the model's prediction of 1.5503 RIU is notably accurate. Positive contributions from features such as 1529.32 nm, 1559.74 nm, and 1524.46 nm drive this high accuracy. These features are crucial for detecting HRI values, as they capture intricate spectral patterns associated with HRI variations. However, features like 1536.34 nm, exhibit diminished effectiveness for HRI detection which possibly due to their sensitivity to LRI values, as evidenced by their negative Shapley values.

Hence, the comparative analysis of Shapley values across LRI and HRI conditions highlights the model's capability to adapt to different RI ranges by leveraging distinct wavelength features. Certain features, such as 1559.74 nm, show robustness across both conditions, reflecting their general applicability in refractive index measurement. In contrast, other features demonstrate specialization, suggesting that different feature sets are optimal for LRI versus HRI detection. In addition, this Shapley-based analysis provides valuable insights into feature contributions, guiding the optimization of the BNN model and sensor design. By focusing on the most influential wavelength features identified through Shapley values, the model's performance can be refined for more accurate RI measurements across various ranges. The analysis underscores the BNN's superior ability to capture and refine complex patterns, contributing to its high performance in both LRI and HRI sensing.

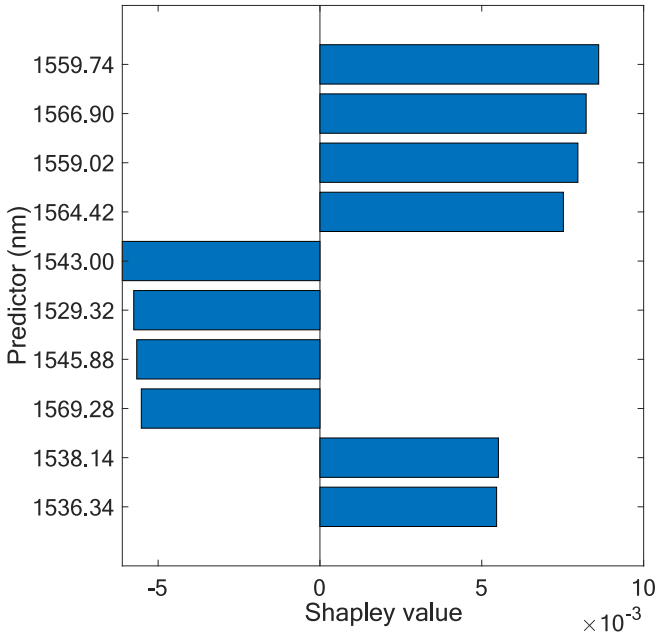

Fig. 12. Bar graph of shapley values for LRI prediction at 1.3000 RIU.

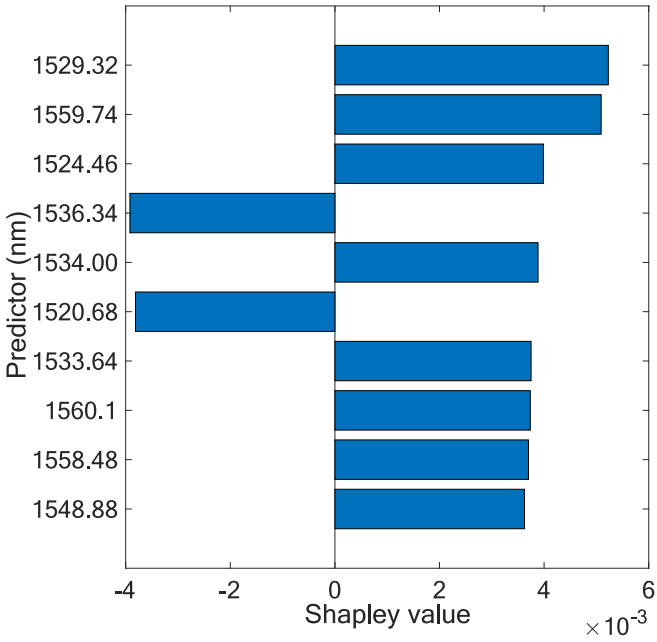

Fig. 13. Bar graph of shapley values for HRI prediction at 1.5500 RIU.

Following the completion of the training process, the remaining 20 % of the data, which had not been used by the BNN regression model during training, was used to evaluate the model's performance. The test dataset results yielded the following metrics with an RMSE of 0.0044, an MSE of 1.9360×10^{-5}, an MAE of 0.0030847, and an R2 score of 0.99698, indicating an impressive regression accuracy approaching to 99.7 %. Table 3 provides a breakdown of the model's accuracy in predicting the RI values, specifically across two RI ranges which are 1.3000 RIU-1.3900 RIU for LRI regime and 1.4600 RIU-1.5500 RIU for HRI regime.

Table 3
Actual and predicted ri values comparison using bnn regression model.

Actual RI Liquid (RIU)	Predicted RI Liquid (RIU)
1.3000	1.3003
1.3100	1.3103
1.3200	1.3202
1.3300	1.3301
1.3400	1.3394
1.3500	1.3498
1.3600	1.3599
1.3700	1.3706
1.3800	1.3795
1.3900	1.3912
1.4600	1.4598
1.4700	1.4707
1.4800	1.4802
1.4900	1.4898
1.5000	1.5000
1.5100	1.5098
1.5200	1.5193
1.5300	1.5298
1.5400	1.5395
1.5500	1.5503

Table 4 provides a summary of previous research on AI-based OFS for RI sensing. A key observation is that most of these studies have focused on LRI sensing, which limits their applicability in situations where a broad RI range is required. Additionally, the sensor designs used in these studies often involve complex fabrication processes and are highly susceptible to temperature variations, compromising their reliability in practical applications. In some implementations of AI-based OFS, it relies on data obtained through simulations rather than actual experiments. This introduces potential bias, as the transmission spectra generated through simulations may not accurately reflect real-world conditions, where environmental factors play a significant role. Recently, a pioneering study introduced the first AI-based approach capable of handling a broad RI range, including both LRI and HRI sensing based on FPI configuration. However, the sensor head design in this study is highly complex and demonstrates significant cross-sensitivity to temperature variations. Additionally, the ML algorithm used is primarily suited for classification tasks, which typically handle categorical outcomes rather than continuous numerical values. Therefore, the data must be preprocessed to extract relevant features, which are then used as inputs for the ML model. This approach may be less effective for more intricate signals, such as those generated by the MMI sensor scheme.

In contrast, this proposed study presents an MMI sensor design with a simple sensor head structure that can be easily fabricated using standard optical communication equipment. This scheme enables precise detection across both LRI and HRI regimes, supported by the BNN model algorithm for accurate signal processing. Instead of using specific signal features as input to the ML model, this work utilizes the entire wavelength spectrum raw data as input. This approach eliminates the need for preprocessing the raw data to identify particular signal features. It is worth noting that the experiments only used Cargille Series A and AAA liquids for RI measurements, which accounts for the lack of data in the 1.4000 RIU to 1.4500 RIU range. However, the sensor is expected to perform effectively within this range as well, given that the response signal trend is likely to follow the same pattern shown in Fig. 7 once the measurements for this range are included. It is also noted that the previous study [32] was dedicated solely to HRI detection, utilizing an SMF-NCF-SMF sensor configuration with a detection range confined to HRI values (1.4600–1.5500 RIU). In contrast, the current work leverages an AI-powered BNN regression model with a similar sensor configuration, enabling precise detection of both LRI and HRI using a single MMI fiber structure. This approach achieves high accuracy of 99.7 %, surpassing the limitations of conventional methods which limit to LRI or HRI only. This advancement paves the way for a wide range of applications in environmental, biomedical, and industrial sensing. Additionally, the proposed sensor exhibits strong immunity to temperature variations due to its all-silica sensing structure [44]. Silica has a low thermo-optic coefficient, offering greater stability compared to germanosilicate-core fibers typically used in single-mode and multimode fiber-based sensor heads.

5. Conclusion

In this work, we have developed a robust and AI-driven approach for precise RI across a broad range, spanning both LRI and HRI conditions. By integrating a MMI fiber sensor with a BNN regression model, we achieved accurate prediction of RI values from 1.3000 RIU to 1.3900 RIU for LRI environments, and from 1.4600 RIU to 1.5500 RIU for HRI conditions. The model demonstrated an accuracy of 99.7 % and a low root mean square error (RMSE) of 0.0044, ensuring that the predicted values closely matched the actual measurements. The MMI sensor design is simple, requiring only fiber cleaving and splicing of a NCF between two single-mode fibers (SMFs), and leverages the interaction of guided and leaky modes for RI sensing. Additionally, the sensor's all-silica NCF structure provides natural resistance to temperature fluctuations, eliminating the need for external temperature compensation mechanisms. This novel approach resolves the complexity and ambiguity typically found in overlapping spectral signals during LRI and HRI measurements in MMI fiber based sensor, making it highly effective for a range of sensing applications. Our method offers a practical, reliable, and accurate solution for RI sensing, suitable for deployment in diverse environmental conditions, and holds significant promise for advancing RI measurement technologies.

CRediT authorship contribution statement

Nurul Farah Adilla Zaidi: Writing – original draft, Validation, Methodology, Investigation, Conceptualization. **Muhammad Yusof Mohd Noor:** Writing – original draft, Validation, Methodology, Investigation, Conceptualization. **Nur Najahatul Huda Saris:** Writing – review & editing, Formal analysis. **Mohd Rashidi Salim:** Methodology, Conceptualization. **Sumiaty Ambran:** Formal analysis. **Azizul Azizan:**

Table 4
AI-based OFS for LRI and HRI sensing.

AI Model & Data Collection Method	Fiber Structure & Fabrication Complexity	RI Range (RIU)	RI Regime	Sensitivity	TCS	Model approach	Year
Polynomial Regression + PCA (Experimental) [39]	Thin gold film coated TFBG-SPR (Very complex)	1.3330–1.3774	LRI	MSE: 1.9×10^{-5}	Yes	Regression	2022
CNN (Experimental) [40]	TFBG (Medium complex)	1.3350–1.3790	LRI	RMSE: – MAE: 4.01×10^{-4} MSE: 2.818×10^{-7} R^2: 0.9982	Yes	Regression	2022
ANN (Simulation) [41]	Ag-grated D-shaped SPR (Very complex)	1.3500–1.3900	LRI	S: 3890 nm/RIU R^2: 0.9684	Yes	Regression	2023
ANN (Simulation) [42]	PCF-based SPR (Very complex)	1.3300–1.4300	LRI	MSE: 0.0097 R^2:0.9987	Yes	Regression	2024
SVM (Experimental) [43]	SMF-cascaded internal mirror SMF-SMF (Very complex)	1.3158–1.5809	LRI & HRI	–	Yes	Classification	2022
BNN (Experimental) [Our work]	SMF-NCF-SMF (Very simple)	1.3000–1.3900 & 1.4600–1.5500	LRI & HRI	RMSE: 0.0044 MAE: 0.0030847 MSE: 1.936×10^{-5} R^2: 0.99698	Negligible	Regression	2024

TCS = Temperature Cross Sensitivity, RI = Refractive Index, AI = Artificial Inteligent, PCA = Principal Component Analysis, CNN = Convolutional Neural Network, ANN = Artificial Neural Network, SVM = Support Vector Machine, BNN = Bilayer Neural Network, LRI – Low Refractive Index, HRI = High Refractive Index.

Methodology, Conceptualization. **Raja Kamarulzaman Raja Ibrahim:** Visualization. **Fauzan Ahmad:** Visualization. **Nurul Ashikin Daud:** Formal analysis. **Norazida Ali:** Formal analysis. **Norizan Mohamed Nawawi:** Visualization. **Ian Yulianti:** Methodology, Conceptualization. **Gang-Ding Peng:** Writing – review & editing, Methodology, Conceptualization.

Declaration of competing interest

The authors declare that they have no known competing financial interests or personal relationships that could have appeared to influence the work reported in this paper.

Acknowledgement

This work was supported by the Ministry of Higher Education under Fundamental Research Grant Scheme, UTM, FRGS/1/2023/TK07/UTM/02/20.

Data availability

The data that has been used is confidential.

References

[1] A. Prasanth, et al., A comparative study of ZnO, AZO, TiO2, Sb2O3, and SnO2 nanomaterials coated SPR based fiber optic refractive index sensors for chemical sensing application, Opt. Mater. 152 (2024) 115438.
[2] R. Rahad, A. Ali, M.K.H. Pias, M. Farabi, M.A. Islam, A.A. Fahim, Plasmonic metal-insulator-metal (MIM) refractive index sensor for glucose level monitoring, Plasmonics (2024) 1–10.
[3] P. Nagarajan, S. Manoharadas, V. Dhasarathan, S. Rajeshkannan, Cancer detection using multi-layered kretschmann configuration–based refractive index sensor, Plasmonics (2024) 1–12.
[4] S.J. Mishu, M.A. Rahman, N. Dhar, Highly sensitive refractive index sensing with a dual-band optically transparent ITO-based perfect metamaterial absorber for biomedical applications, Heliyon 10 (5) (2024).
[5] I. 60814, Insulating liquids—Oil-impregnated paper and pressboard—Determination of water by automatic coulometric Karl Fischer titration, IEC 60814 (1997) 1997.
[6] J. Wekalao, S.K. Patel, O. Alsalman, J. Surve, N. Anushkannan, J. Parmar, Waterborne bacteria detecting highly sensitive graphene metasurface based cost-efficient and efficient refractive index sensors, Plasmonics 19 (1) (2024) 347–361.
[7] R. Fu, et al., Optical fiber sensors for heavy metal ion sensing, J. Mater. Sci. Technol. (2024).
[8] G. Han, High-performance fibre-based and silicon photonics-based optical frequency domain reflectometry for battery sensing, University of Southampton, 2024.
[9] L.A. Ngiejungbwen, H. Hamdaoui, M.-Y. Chen, Polymer optical fiber and fiber Bragg grating sensors for biomedical engineering Applications: A comprehensive review, Opt. Laser Technol. 170 (2024) 110187.
[10] E. Dejband, T.-H. Tan, C.-K. Yao, E.-M. Chang, P.-C. Peng, Enhancing multichannel fiber optic sensing systems with IFFT-DNN for remote water level monitoring, Sensors 24 (15) (2024) 4903.
[11] M. Aledhari, R. Razzak, B. Qolomany, A. Al-Fuqaha, F. Saeed, Biomedical IoT: enabling technologies, architectural elements, challenges, and future directions, IEEE Access 10 (2022) 31306–31339.
[12] R. Kuang, et al., "Smart photonic wristband for pulse wave monitoring, Opto-Electron. Sci. (2024), pp. 240009-1-240009-16.
[13] K. Karipbayeva, W. Blanc, D. Tosi, Optical fiber semi-distributed interferometer assisted by an FBG for thermorefractometry and sweat sensing, IEEE Sens. J. 23 (13) (2023) 14161–14166.
[14] Y. Du, B. Sun, J. Li, W. Zhang, Optical Fiber Sensing and Structural Health Monitoring Technology, Springer, 2019.
[15] L. Jiao, N. Zhong, X. Zhao, S. Ma, X. Fu, D. Dong, Recent advances in fiber-optic evanescent wave sensors for monitoring organic and inorganic pollutants in water, TrAC Trends Anal. Chem. 127 (2020) 115892.
[16] M. Leone, Advances in fiber optic sensors for soil moisture monitoring: A review, Results Opt. 7 (2022) 100213.
[17] Y. Su, Y. Du, W. Wang, L. Xu, S. Dai, P. Zhang, S-shaped tellurite optical fiber surface plasmon resonance sensor for temperature and refractive index measurement, Opt. Laser Technol. 179 (2024) 111385.
[18] S. Ullah, et al., Dual-side polished surface plasmon resonance–based photonic crystal fiber for refractive index sensing and polarization filtering, Plasmonics (2024) 1–11.
[19] C. Duan, J. Li, K. Zhang, M. Tian, Optical fiber dual-parameter sensors based on different kinds of interferometers for measuring refractive index and temperature: a review, Opt. Quant. Electron. 56 (2) (2024) 262.
[20] S. Duan, et al., All in-fiber Fabry–Pérot interferometer sensor towards refractive index and temperature simultaneous sensing, Opt. Laser Technol. 180 (2025) 111551.
[21] Y. Chen, L. Yue, X. Yang, C.L. Jones, Z. Wang, Superlens-Assisted laser nanostructuring of Long Period optical fiber Gratings (LPGs) for enhanced refractive index sensing, Opt. Laser Technol. 176 (2024) 111001.
[22] J. Chen, S. Cui, S. Zhang, A. Liu, Refractive index sensors based on a chirped core long-period fiber grating, IEEE Photon. Technol. Lett. (2024).
[23] J. Wang, X. Chen, X. Li, Y. Chen, Fiber optic refractive index sensor based on U-Tapered structure, vol. 13179, in: International Conference on Optics and Machine Vision (ICOMV 2024), SPIE, 2024, pp. 112–117.
[24] S.K. Abbas, S.S. Ahmed, Refractive index sensor based on tapered photonic crystal fiber to determine the performance of different carbonated liquids, J. Opt. 53 (3) (2024) 2726–2730.
[25] W. Zheng, B. Han, Y.-N. Zhang, L. Liu, Y. Zhao, An in-fiber sensor for simultaneous measurement of cholesterol concentration and temperature based on SPR and MMI, Anal. Chim. Acta 1287 (2024) 342043.
[26] Y. Li, X. Li, Y. Liu, J. You, Y. Peng, H. Chen, High sensitivity Mach-Zehnder interferometric fiber-optic humidity sensor based on multimode interference enhancement, Opt. Fiber Technol. 87 (2024) 103891.
[27] H. Qiu, W. Li, C. Zhu, J. Xu, J. Li, G. Bai, A high-sensitivity D-shaped photonic crystal fiber surface plasmon resonance sensor for low refractive index detection, J. Opt. 53 (3) (2024) 1897–1905.
[28] X. Yang, et al., D-shaped photonic crystal fiber based on surface plasmon resonance for low refractive index applications, Opt. Mater. (2024) 115612.
[29] C.E. Domínguez-Flores, O. Rodríguez-Quiroz, D. Monzón-Hernández, Simple signal processing method to enlarge the dynamic range of the Fresnel reflection-based fiber Fabry–Pérot refractive index sensors, J. Lightwave Technol. 39 (5) (2021) 1497–1503.
[30] O. Rodríguez-Quiroz, C.E. Domínguez-Flores, D. Monzón-Hernández, C. Moreno-Hernández, Hybrid fiber fabry–perot interferometer with improved refractometric response, J. Lightwave Technol. 37 (17) (2019) 4268–4274. Available: https://opg.optica.org/jlt/abstract.cfm?URI=jlt-37-17-4268.
[31] L.-S. Huang, G.-R. Lin, M.-Y. Fu, H.-J. Sheng, H.-T. Sun, W.-F. Liu, A refractive-index fiber sensor by using no-core fibers, in: 2013 International Symposium on Next-Generation Electronics, IEEE, 2013, pp. 100–102.
[32] N.F.A. Zaidi, N.N.H. Saris, M.Y.M. Noor, S. Ambran, M.R. Salim, M.H. Ibrahim, Investigation of transformer oil aging using no-core optical fiber (NCF) sensor, Phys. Scr. 99 (9) (2024) 095507.
[33] A.-N. Sharkawy, Principle of neural network and its main types, J. Adv. Appl. Comput. Math. 7 (2020) 8–19.
[34] J.-S. Pan, Z. Zhang, S.-C. Chu, S.-Q. Zhang, J.-M.-T. Wu, A parallel compact Marine Predators Algorithm applied in time series prediction of Backpropagation neural network (BNN) and engineering optimization, Math. Comput. Simul 220 (2024) 65–88.
[35] J. Chen, K. Li, K. Bilal, K. Li, S.Y. Philip, A bi-layered parallel training architecture for large-scale convolutional neural networks, IEEE Trans. Parallel Distrib. Syst. 30 (5) (2018) 965–976.
[36] L.B. Soldano, E.C. Pennings, Optical multi-mode interference devices based on self-imaging: principles and applications, J. Lightwave Technol. 13 (4) (1995) 615–627.
[37] Q. Wang, C. Li, C. Zhao, W. Li, Guided-mode-leaky-mode-guided-mode fiber interferometer and its high sensitivity refractive index sensing technology, Sensors 16 (6) (2016) 801.
[38] L. Yang, L. Xue, D. Che, J. Qian, Guided-mode-leaky-mode-guided-mode fiber structure and its application to high refractive index sensing, Opt. Lett. 37 (4) (2012) 587–589.
[39] E.D. Chubchev, K.A. Tomyshev, I.A. Nechepurenko, A.V. Dorofeenko, O.V. Butov, Machine learning approach to data processing of TFBG-assisted SPR sensors, J. Lightwave Technol. 40 (9) (2022) 3046–3054.
[40] Z. Cao, et al., Improved spectral interrogation of tilted fiber Bragg grating refractometer using residual convolutional neural networks, J. Lightwave Technol. 40 (22) (2022) 7403–7411.
[41] Y. Dogan, R. Katirci, İ. Erdogan, E. Yartasi, Artificial neural network based optimization for Ag grated D-shaped optical fiber surface plasmon resonance refractive index sensor, Opt. Commun. 534 (2023) 129332.
[42] M. Al Mahfuz, S. Afroj, A. Rahman, M.A. Hossain, M.A. Hossain, M.S. Habib, Ultra-sensitive visible-IR range fiber based plasmonic sensor: a finite-element analysis and deep learning approach for RI prediction, IEEE Access (2024).
[43] R. Martínez-Manuel, L.M. Valentín-Coronado, J. Esquivel-Hernández, K.-J.-J. Monga, S. LaRochelle, Machine learning implementation for unambiguous refractive index measurement using a self-referenced fiber refractometer, IEEE Sens. J. 22 (14) (2022) 14134–14141.
[44] B. Song, Y. Miao, W. Lin, H. Zhang, J. Wu, B. Liu, Multi-mode interferometer-based twist sensor with low temperature sensitivity employing square coreless fibers, Opt. Express 21 (22) (2013) 26806–26811.